# Magnetic circular dichroism spectra of transition metal complexes calculated from restricted active space wavefunctions



| | |
|---|---|
| Journal: | *Physical Chemistry Chemical Physics* |
| Manuscript ID | CP-ART-12-2018-007849.R1 |
| Article Type: | Paper |
| Date Submitted by the Author: | 07-Feb-2019 |
| Complete List of Authors: | Heit, Yonaton ; University at Buffalo - The State University of New York<br>SERGENTU, Dumitru-Claudiu; University at Buffalo - The State University of New York, Chemistry<br>Autschbach, Jochen; University at Buffalo, State University of New York, Chemistry |
| | |

# Magnetic circular dichroism spectra of transition metal complexes calculated from restricted active space wavefunctions

Yonaton Heit,[†] Dumitru-Claudiu Sergentu[†] and Jochen Autschbach[*]

Department of Chemistry
University at Buffalo
State University of New York
Buffalo, NY 14260-3000, USA
email: jochena@buffalo.edu

**Abstract** First principles multiconfigurational restricted active space (RAS) self-consistent field (SCF) or configuration interaction (CI) approaches, augmented with a treatment of spin-orbit coupling by state interaction, were used to calculate the magnetic circular dichroism (MCD) $\mathcal{A}$-, $\mathcal{B}$-, and/or $\mathcal{C}$-terms for closed- and open-shell transition metal complexes: $PdCl_4^{2-}$, $PdBr_4^{2-}$, $AuCl_4^-$, $AuBr_4^-$, $MnO_4^-$, $CuCl_4^{2-}$, $CuBr_4^{2-}$, and $Fe(CN)_6^{3-}$. The $\mathcal{B}$-terms were determined with a sum-over-states approach. It is shown that accurate MCD spectra can be obtained directly at a RAS level or at a RAS level augmented with corrections for the dynamic correlation. The sign and magnitude of the individual MCD terms can be unambiguously determined and assigned to particular electronic transitions.

## 1 Introduction and Theory

Magnetic circular dichroism (MCD)[1] is the differential absorption of left vs. right-circularly polarized light in the presence of a static magnetic field of the same direction as the propagation direction of the light wave. Unlike natural circular dichroism (CD), which requires a chiral medium such as a solution of a chiral molecule with enantiomeric excess, MCD can be induced in non-chiral molecules. The technique is in widespread use to study electronic transitions, predominantly in the UV-Vis range, as a complement to standard absorption spectroscopy. MCD gives information about the nature and degeneracy of the electronic states involved in the transitions, and their magnetic properties. In regions with overlapping bands, MCD may be able to reveal information about the contributing states that is hidden in the absorption spectrum,[2] because the MCD intensities of different transitions may have different signs or band shapes. MCD has been applied, for instance, to probe the electronic structure of transition metal complexes,[3–10] metal clusters,[11,12] mesogenic organic materials,[13] and polycyclic aromatic organic molecules,[14] to characterize active sites in bio-chemical systems,[15–20] to model vibronic coupling of organic molecules,[21,22] and to study systems containing lanthanides and actinides.[23–30]

The quantum theoretical foundation of MCD was developed by Buckingham and Stephens[31,32] and further elaborated by Piepho & Schatz.[1] Under the Born-Oppenheimer approximation, the assumption that the Zeeman splitting of the electronic states is small compared to $k_B T$ and the

transition energy, the assumption that the magnetic field $\boldsymbol{B}$ does not change the absorption line shape, and by treating the $\boldsymbol{B}$-field with perturbation theory to first order, the MCD intensity for an electronic transition $|A\rangle$ to $|J\rangle$ is given by

$$\frac{\Delta\varepsilon}{E} = \gamma B \left[ -\mathcal{A} \left( \frac{\partial f(E)}{\partial E} \right) + \left( \mathcal{B} + \frac{\mathcal{C}}{k_B T} \right) f(E) \right] \tag{1}$$

where $\Delta\varepsilon$ is the differential molar absorption coefficient for left and right polarized light, $E$ is the energy of the light inducing the transition, and $f(E)$ a line shape function. The factor $\gamma$ is

$$\gamma = \frac{2\mu_B N_A \pi^3 \log_{10} e}{250hc} \tag{2}$$

in Gaussian units. Here, $\mu_B$ is the Bohr magneton, $N_A$ is the Avogadro constant, $h$ is Planck's constant, and $c$ is the speed of light. A Lorentz field factor in order to account for a medium is commonly included in the expression for the MCD intensity but has been omitted here, as medium effects can be modeled in quantum chemical calculations more specifically, if needed.

Per Equation 1, the intensity of a transition in the MCD spectrum can be separated into so called $\mathcal{A}$-, $\mathcal{B}$-, and $\mathcal{C}$-terms. Diamagnetic molecules exhibit temperature-independent $\mathcal{A}$- and $\mathcal{B}$-terms. Molecules with a paramagnetic ground state (GS) may additionally exhibit $\mathcal{C}$-terms, which have a $1/(k_B T)$ temperature-dependence and tend to dominate the MCD spectra particularly at low temperatures. The $\mathcal{C}$-term $1/(k_B T)$ factor arises from the linearization of the Boltzmann factors when calculating the population difference of the GS components when they are subjected to the Zeeman splitting by the external $\boldsymbol{B}$-field. The $\mathcal{B}$-terms are generally present and arise from the mixing of zero-field states in the presence of the magnetic field. $\mathcal{A}$-terms appears for degenerate excited states (ESs) subject to Zeeman splitting. If the $\mathcal{B}$- and $\mathcal{C}$-term bands are described by a band shape function $f(E)$ (such as a Gaussian or Lorentzian band shape), then the $\mathcal{A}$-term has a characteristic $\partial f(E)/\partial E$ derivative band shape. The expressions for the isotropic $\mathcal{A}$-, $\mathcal{B}$-, and $\mathcal{C}$-term for a transition $|A\rangle$ to $|J\rangle$ as given by Piepho and Schatz[1] are

$$\begin{aligned} \mathcal{A} \;=\; & \frac{i}{3|A|} \sum_{\alpha,\alpha'} \sum_{\lambda\lambda'} \Big( \langle J\lambda | \boldsymbol{L} + 2\boldsymbol{S} | J\lambda' \rangle \, \delta_{\alpha\alpha'} \\ & + \langle A\alpha' | \boldsymbol{L} + 2\boldsymbol{S} | A\alpha \rangle \, \delta_{\lambda\lambda'} \Big) \cdot \langle A\alpha | \boldsymbol{\mu} | J\lambda \rangle \times \langle J\lambda | \boldsymbol{\mu} | A\alpha \rangle \end{aligned} \tag{3}$$

$$\mathcal{B} = \frac{2}{3|A|}\,\mathrm{Im}\sum_{\alpha\lambda}\Big[\sum_{K\neq A}\sum_{\kappa}\frac{\langle K\kappa|\boldsymbol{L}+2\boldsymbol{S}|A\alpha\rangle}{E_K-E_A}\cdot\langle A\alpha|\boldsymbol{\mu}|J\lambda\rangle\times\langle J\lambda|\boldsymbol{\mu}|K\kappa\rangle + \sum_{K\neq J}\sum_{\kappa}\frac{\langle J\lambda|\boldsymbol{L}+2\boldsymbol{S}|K\kappa\rangle}{E_K-E_J}\cdot\langle A\alpha|\boldsymbol{\mu}|J\lambda\rangle\times\langle K\kappa|\boldsymbol{\mu}|A\alpha\rangle\Big] \tag{4}$$

$$\mathcal{C} = \frac{i}{3|A|}\sum_{\alpha\alpha'}\sum_{\lambda}\langle A\alpha|\boldsymbol{L}+2\boldsymbol{S}|A\alpha'\rangle\cdot\langle A\alpha|\boldsymbol{\mu}|J\lambda\rangle\times\langle J\lambda|\boldsymbol{\mu}|A\alpha'\rangle \tag{5}$$

Here, $|A|$ is the degeneracy of the GS, and $\alpha$, $\lambda$, and $\kappa$ are components of the GS, the ES, and intermediate states $K$, respectively. Further, $\boldsymbol{L}$ and $\boldsymbol{S}$ are dimensionless one-electron orbital and spin angular momentum operators, and $\boldsymbol{\mu}$ is the one-electron electric dipole operator. The $E_A$, $E_J$, and $E_K$ are the state energies in the absence of the magnetic field. Finally, $\cdot$ and $\times$ indicate scalar and cross products of the dipole vector matrix elements.

MCD $\mathcal{A}$- and $\mathcal{B}$-term spectra of diamagnetic systems can be calculated efficiently with time-dependent Kohn-Sham theory (TD-KST).[14,22,33–41] A recent interesting application is the assignment of MCD spectra of ligand-protected gold clusters.[11,12] These methods require a quadratic response step in order to obtain the $\boldsymbol{B}$-field perturbed excitation energies and transition density matrices, respectively. Coriani et al. developed correlated wavefunction methods to calculate these two terms.[42] $\mathcal{C}$-terms of transition metal complexes have been investigated with KST calculations as well,[43,44] but the approach has limitations due to the known problems of KST with open-shell systems. Multi-reference wavefunction based $\mathcal{C}$-term calculations were performed, for instance, by Bolvin,[45] Ganyushin and Neese,[46] Ye et al.,[6,47] and Gendron et al.[30] In References 30 and 45 the same computational approach was used, namely the explicit determination of electric and magnetic transition dipole moments and excitation energies from restricted active space (RAS) wavefunction calculations, with (RAS-SCF) or without (RAS-CI) orbital optimization, and spin-orbit (SO) coupling treated via state interaction of RAS spin states.

In the present work, the applicability of RAS-level approaches to calculate MCD spectra of closed-shell and open-shell 3d, 4d, and 5d metal complexes is explored. We show that MCD spectra of reasonable quality can be obtained at the RAS-level directly, or at a RAS-level with corrections to the state energies due to the dynamic electron correlation obtained from second-order perturbation theory (PT2) or multi-configurational pair density functional theory (MC-pDFT). For the $\mathcal{B}$-terms, a sum-over-states (SOS) approach is used in a basis of a comparatively large set of states determined by RAS-CI calculations, using an orbital basis optimized in a previous RAS-SCF calculation with a smaller active space suitable for the valence states in the UV-Vis region. $\mathcal{A}$- and $\mathcal{B}$-term spectra are presented and analyzed for $PdCl_4^{2-}$, $PdBr_4^{2-}$, $AuCl_4^{-}$, $AuBr_4^{-}$ (closed-shell $d^8$ complexes), and $MnO_4^{-}$ ($d^0$). $\mathcal{C}$- term spectra are presented and analyzed for $CuCl_4^{2-}$ and

$CuBr_4^{2-}$ ($d^9$). Finally, a spectrum containing contributions from all three terms is presented for the challenging complex $Fe(CN)_6^{3-}$ (low-spin $d^7$). This orbitally degenerate iron complexes is treated by the RAS approach as well as the other systems.

## 2 Computational Details

For all complexes, structure optimizations were performed with KST using all-electron doubly-polarized triple-$\zeta$ (TZ2P) Slater-type basis sets,[48] and the zeroth order regular approximation (ZORA) all-electron relativistic Hamiltonian,[49] using the 2017 release of the Amsterdam Density Functional (ADF) package.[50] Time-dependent KST (TD-KST) linear response calculations were performed at the same level in order to generate absorption spectra for comparison with the wavefunction calculations. All KST calculations utilized the CAM-B3LYP functional.[51] Scalar-relativistic (SR) ZORA was used for all optimizations as well as for the TD-KST calculations on the closed-shell systems, while two-component spin-orbit (SO) ZORA was used for the TD-KST calculations on the open-shell systems. Results obtained with SO-ZORA will be referenced as TD-KST+SO. The conductor-like screening solvation model was used to treat solvent effects from water for the $d^8$ complexes and $MnO_4^-$, and from acetonitrile for the $d^9$ complexes. Calculated vs. experimental (crystal structure) metal-ligand bond lengths, which are in good agreement, are compiled in Table S1 of the Supporting Information (SI) file. The optimized structures are expected to describe better the solution structures for which MCD was recorded and therefore they were used for the single-point wavefunction calculations.

RAS-level calculations were performed with the second-order Douglas-Kroll-Hess (DKH2) all-electron relativistic Hamiltonian[52–55] and ANO-RCC-VTZP basis sets,[56,57] using a developer's version of Molcas (pre v8.1) and OpenMolcas.[58] The $D_2$ symmetry point group was used for all complexes except $Fe(CN)_6^{3-}$, for which $D_{2h}$ was used. Note that the full symmetry point groups are $T_d$ for $MnO_4^-$, $D_{4h}$ for the $d^8$ complexes and $D_{2d}$ for the $d^9$ complexes. The conductor-like polarizable continuum model (C-PCM)[59,60] was used to account for solvent effects (water or acetonitrile) for all the studied complexes unless otherwise specified.

Dynamic correlation was addressed with multi-reference PT2[61] calculations that made use of a 0.2 / 0.3 a.u. imaginary shifts for the $d^9$ / $d^8$ complexes to eliminate intruder states. Calculations on $Fe(CN)_6^{3-}$ are challenging, as since this system exhibits low-energy ligand-to-metal charge transfer (LMCT) states that are governed by strong static and dynamic correlation. A proper modeling of these states requires a large active space and an advanced method for the dynamic correlation.[46] In this work, more reasonable results compared to the experimental MCD spectrum were obtained with multiconfigurational density functional theory (MC-pDFT) and the on-top TLSDA density functional recently developed by Gagliardi et al.[62]

For the closed-shell $d^8$ complexes, the orbitals were optimized in a state-averaged RAS-SCF fashion with the RAS1 space containing the twelve valence $n$p ($n$ = 3, 4) ligand orbitals with 24 electrons and at most two holes, and the RAS2 space containing the five valence $n$d ($n$ = 4, 5) metal orbitals and 8 electrons. In $D_2$, 45 spin-singlet states were calculated in the $A_1$ irreducible representation (irrep) and 36 spin-singlet states were calculated in each of the remaining irreps. A RAS-CI calculation was subsequently performed with the $(n+1)$s and $(n+1)p_z$ metal orbitals added to RAS3. At maximum two holes / one electron was allowed in RAS1 / RAS3 while 575 and 566 spin-singlet states were calculated in $A_1$ and respectively each of the remaining irreps. Using the RAS-SCF or the RAS-CI wavefunctions, dynamic correlation is introduced with PT2 and the results will be referenced as PT2//SCF and respectively PT2//CI. It is worth mentioning that the CI treatment of additional states using pre-optimized orbitals, as in PT2//CI, did not lead to deterioration of the absorption spectra (see Figures 2 and 3). Test calculations showed that there is hardly any mixing between spin-singlet and spin-triplet states below 200,000 $cm^{-1}$ due to spin-orbit coupling (SOC). Therefore, spin-triplet states were not accounted for in the MCD calculations for the closed-shell complexes.

In principle, an infinite number of states are required for the $\mathcal{B}$-term SOS. For practical reasons, spin-singlet states with an energy below 120,000 $cm^{-1}$ at the RAS level were retained for the MCD calculations. Figure S5 of the Supporting Information (SI) shows for the $d^8$ complexes that the $\mathcal{B}$ terms are well converged with respect to the number of states considered for the SOS of Equation 4. In our test calculations, we found that the $\mathcal{B}$ terms converge quickly with the number of states, and the quality of the additional states does not appear to be critical in order to obtain reasonable MCD $\mathcal{B}$-term spectra. There appears to be a similarity to magnetic susceptibility calculations, which are also known to converge rather quickly with the number of states and not being particularly sensitive to the dynamic correlation.[63–65]

For the $d^9$ complexes, GS state-specific calculations were initially performed. The RAS2 space included the ten 3d and double-shell 3d′ metal orbitals, and the bonding $3b_1$ orbital (see Figure S2 for visualizations of the $CuCl_4^{2-}$ orbitals).[66] Subsequently, a RAS-CI calculation was performed with RAS1 containing 12 $n$p ($n$ = 3, 4) ligand orbitals with 24 electrons and at most two electron holes, RAS2 containing the five 3d orbitals with 9 electrons, and RAS3 containing the five 3d′ orbitals with at most two electrons. Five spin-doublet states were calculated in irrep A and 4 spin-doublet states were calculated in each of the remaining irreps. Since the $\mathcal{C}$-terms strongly dominate the MCD spectra at low temperature, additional states were not calculated to model $\mathcal{B}$-terms. Again, the RAS-CI wavefunctions were further used in PT2 calculations.

For $MnO_4^-$, an active space was constructed following Su et al.[67] and Sharma et al.[68] It comprised a RAS2 containing the O 2p orbitals with 24 electrons and at maximum four electron-holes, and a RAS3 containing the Mn 3d orbitals with at maximum four electrons. A total of 50 spin-

singlet states were calculated in each irrep of $D_2$ .

For $Fe(CN)_6^{3-}$, the orbitals were initially optimized for one state in each of the $b_{1g}$, $b_{2g}$ and $b_{3g}$ irreps and for three states in each of the $b_{1u}$, $b_{2u}$ and $b_{3u}$ irreps. The active space comprised a RAS2 with nine $CN_\pi$ orbitals from the $b_{1u}$, $b_{2u}$ and $b_{3u}$ irreps (orbitals that span the $t_{1u}$, and $t_{2u}$ irreps of $O_h$), two metal-ligand $\sigma$ bonding orbitals from the $a_g$ irrep ($e_g$ in $O_h$), and the three 3d orbitals from the $b_{1g}$, $b_{2g}$ and $b_{3g}$ irreps ($t_{2g}$ in $O_h$). This active space is close to the one devised by Ganyushin et al,[46] and was exploited herein to describe particularly the three absorption bands occurring between 22000 and 39000 $cm^{-1}$. The converged orbitals for each irrep where then used to perform RAS-CI calculations with an active space that additionally included the two 3d $a_g$ orbitals, with at most one electron, in a RAS3. Note that this extension was necessary to allow for the calculation of a larger number of states needed for the $\mathcal{B}$-terms. In total, 49 spin doublet states were calculated in each of the $b_{1g}$, $b_{2g}$ and $b_{3g}$ irreps and 51 doublet states in each of the $b_{1u}$, $b_{2u}$ and $b_{3u}$ irreps. No spin-quartet states were calculated since they essentially do not mix with the targeted spin-doublet states via SOC. See also Reference 46.

Broadened vertical absorption and MCD spectral envelopes were generated from the calculated state energies, oscillator strengths, and the values for $\mathcal{A}$, $\mathcal{B}$, and $\mathcal{C}$ for each transition. An in-house program previously developed for a different study[30] was used to generate the $\mathcal{C}$ terms. New programs were written for the present work to be able to generate the $\mathcal{A}$ and $\mathcal{B}$ terms and convert the data to yield broadened spectra. This software will be available in the near future as open source.[69] The broadened spectra are based on Equation (1) after rearranging for the molar ellipticity per magnetic field unit, $[\theta]/B$. Useful details about unit conversions related to Equation (1) were provided, for example, by Seth et al.[34,35,37,44] With the magnetic field in Gauss, $[\theta]$ in deg $cm^2$/dmol, and all other quantities in Hartree atomic units, the conversion is $[\theta]/B = 0.0014083E[-\mathcal{A}(\partial f(E))/(\partial E) + \mathcal{B}f(E) + \mathcal{C}/(k_BT)f(E)]$. Normalized Gaussian functions were used for $f(E)$ centered on each transition energy; the corresponding $\sigma$ values are listed in the captions of the figures in Section 3 showing the spectra. The experimental spectra shown in this work were digitized from graphical material in the relevant publications. In older literature, the unit conventions used for the MCD are not always clear, and we have opted to present all spectra in arbitrary units. This means that the presented absorption spectra are proprtional to $\varepsilon$, and the MCD spectra are proportional to $\Delta\varepsilon$ or the molar ellipticity $[\theta]$ per magnetic field unit.

## 3 Results and Discussion

In the text below, band peak energies and calculated state energies relative to the GS are given as photon wavenumbers in units of $10^3$ $cm^{-1}$. These units are abbreviated as trcm, meaning 'thousand reverse (i.e. inverse) cm'.

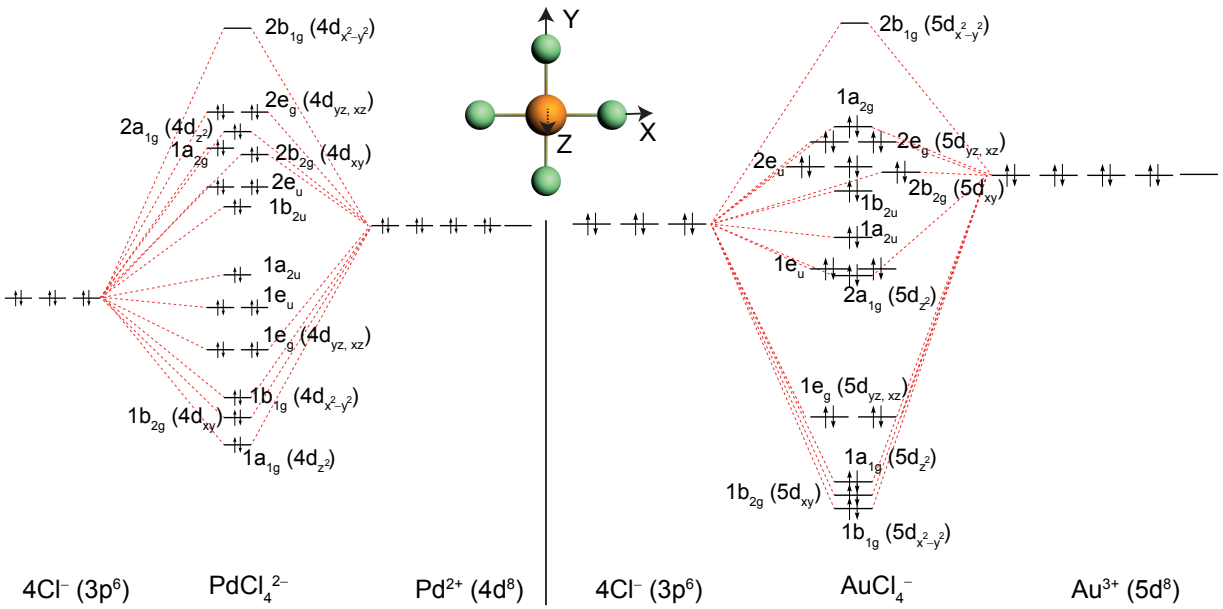


Figure 1: Valence MO diagrams for solvated $PdCl_4^{2-}$ (left) and $AuCl_4^-$ (right). The MO levels were obtained from KST and are drawn to scale. Symmetry labels according to the $D_{4h}$ point group. Selected metal-ligand bonding and antibonding MOs are labeled according to the contributing metal orbital.

### 3.1 Absorption and MCD spectra of $d^8$ complexes

Valence molecular orbital (MO) diagrams of $PdCl_4^{2-}$ and $AuCl_4^-$ are shown in Figure 1. These diagrams are representative for the $PdBr_4^{2-}$ and $AuBr_4^-$ systems as well. Iso-surfaces of the corresponding MOs of $PdCl_4^{2-}$ (which are representative for all four $d^8$ complexes), obtained at the RAS level, are shown in the SI Figure S1. In the presence of the $D_{4h}$ ligand field (LF), the valence *n*d metal orbitals split into $a_{1g}$ ($d_{z^2}$ in the coordinate system shown in Figure 1), $b_{1g}$ ($d_{x^2-y^2}$), $b_{2g}$ ($d_{xy}$), and $e_g$ ($d_{xz}$, $d_{yz}$) metal-ligand bonding and antibonding MO pairs. In the diagrams in Figure 1, these MOs are labeled by the contributing metal d orbital, with the bonding MO of a given pair being at lower energy. For all complexes, the $b_{1g}$ orbital corresponds to the lowest unoccupied MO (LUMO) and the closed shell GS is $^1A_{1g}$. In the energetic range of the occupied valence metal d - ligand combinations there are also occupied ligand-based MOs derived from Cl 3p or Br 4p atomic orbital (AO) combinations of $e_u$, $b_{2u}$ and $a_{2u}$ symmetry. Due to the presence of the inversion center, only transitions from the $^1A_{1g}$ GS to ungerade $^1$LMCT states are dipole-allowed and contribute strongly to the experimentally observed absorption bands. We focus here on the absorption region for which intense bands are present in the experiments, i.e. between about 25 and 50 trcm.[70]

Calculated absorption and MCD spectra for the $d^8$ complexes are shown in Figures 2 and

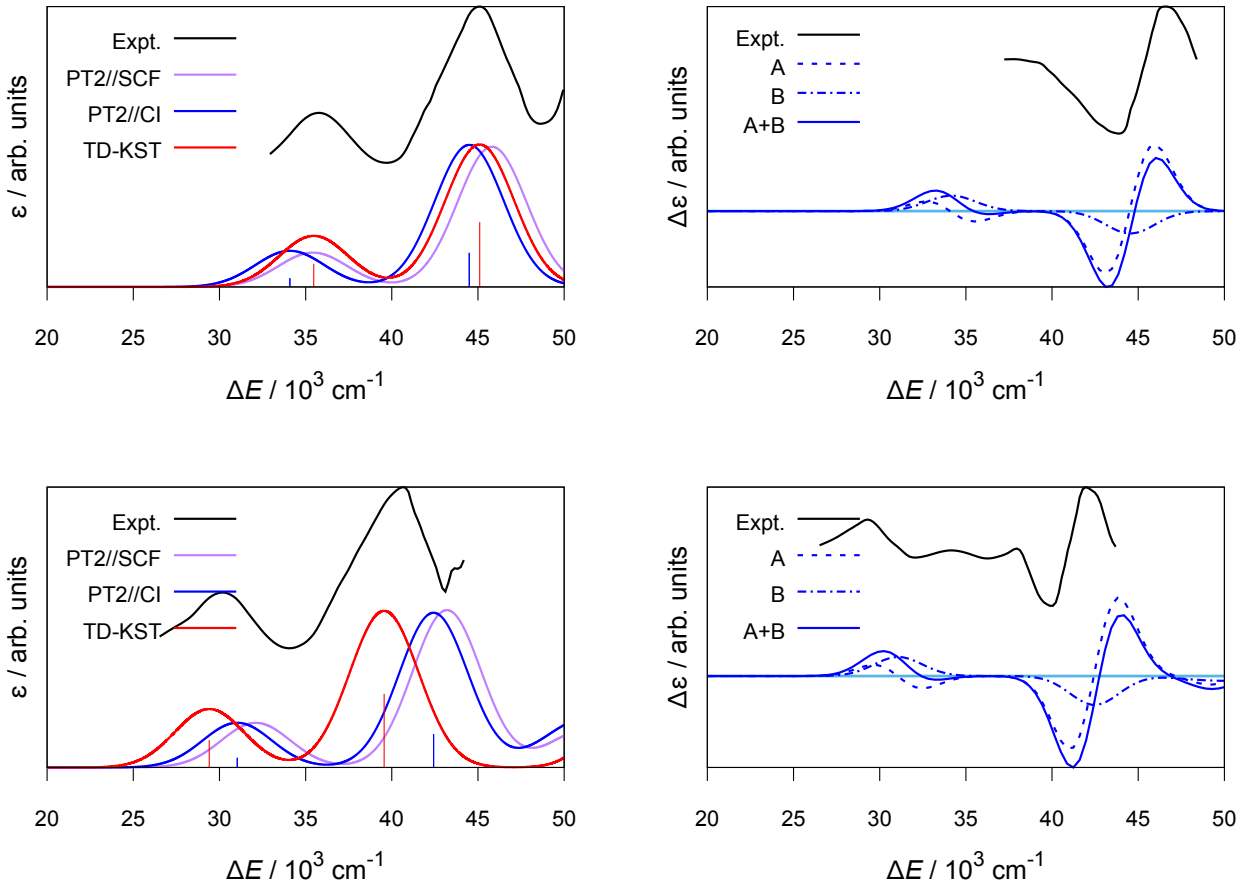


Figure 2: Calculated vs. experimental[70] absorption (left) and MCD (right) spectra of $PdCl_4^{2-}$ (top) and $PdBr_4^{2-}$ (bottom). The calculated MCD spectra are with PT2//CI. The spectra were produced with a Gaussian broadening of 2000 $cm^{-1}$ for the individual transitions.

3. Numerical data are provided in Tables 1 and S2. In agreement with the experiments, both the RAS-level and the TD-KST calculations predict two absorption bands in the region below 50 trcm. These bands are mainly due to $^1A_{1g} \rightarrow {}^1E_u$ LMCT transitions, i.e. excitations from ligand-based $e_u$ orbitals to the $2b_{1g}$ ($d_{x^2-y^2}$) LUMO. An excitation from the ligand-based $1b_{2u}$ orbital to the $2b_{1g}$ LUMO gives rise to a $^1A_{2u}$ LMCT state that is nearly degenerate with the lowest $^1E_u$ LMCT state. The $^1A_{2u}$ transition is in principle also dipole allowed, but in the calculations it has weak intensity. The band assignments are consistent with McCaffery et al.,[70] Jørgensen[71] and others.[72–74] Beyond 50 trcm, absorption bands arise due to transitions from the $^1A_{1g}$ GS to LMCT states via transitions to the lowest-energy unoccupied metal s ($a_{1g}$) or $p_z$ ($a_{2u}$) orbital. The onsets of the corresponding bands are barely visible in the experimental absorption spectra and not resolved in the MCD spectra. Therefore, we do not provide further assignments. However, these states (not shown in Figures 2 and 3) were calculated because of their potential contributions to the MCD $\mathcal{B}$-term bands below 50 trcm.

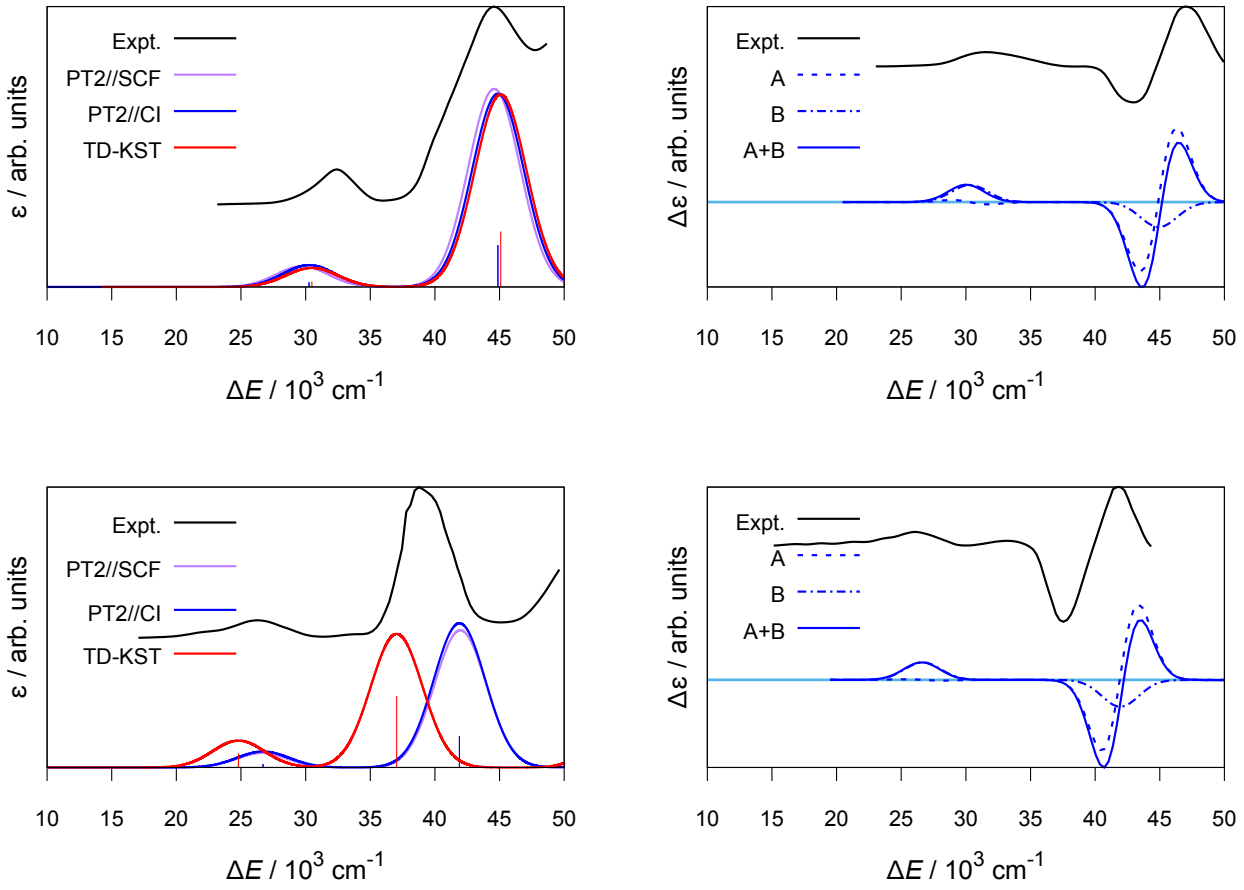


Figure 3: Calculated vs. experimental[70] absorption (left) and MCD (right) spectra of $AuCl_4^{2-}$ (top) and $AuBr_4^{2-}$ (bottom). The calculated MCD spectra are with PT2//CI. The spectra were produced with a Gaussian broadening of 2000 $cm^{-1}$ for the individual transitions.

In the calculated MCD spectra of the $d^8$ complexes there is a moderately strong positive band corresponding to the absorption band around or below 35 trcm (Figures 2 and 3). This MCD band identifies predominantly with a $\mathcal{B}$-term and is generated mainly by the transition to $^1E_u$. The contribution from a $\mathcal{B}$ term of the $^1A_{2u}$ transition is very minor except for $AuBr_4^-$ (see the PT2//CI data in Table 1), due to the small electric transition dipole of this transition. For the Pd complexes, the $\mathcal{B}$-term of the first $^1E_u$ transition overshadows a small positive/negative bisignate feature identifying with a negative $\mathcal{A}$-term of the $^1E_u$ transition. $\mathcal{A}$-terms are also present in the first MCD bands of the gold complexes, but even weaker than for the Pd complexes (Table 1). In the experimental MCD, the $^1E_u$ $\mathcal{A}$-term is only visible in the 30 to 35 trcm region for $PdBr_4^{2-}$. Moreover, only for $PdBr_4^{2-}$, a negative $\mathcal{B}$-term following the $^1E_u$ $\mathcal{A}$-term is also resolved. According to the calculations, this $\mathcal{B}$-term is definitely due to the $^1A_{2u}$ transition (see Table 1) but it does not appear in the PT2//CI spectrum since it is enveloped by the strong positive $^1E_u$ $\mathcal{B}$-term band.

The experimental MCD spectrum[70] of $PdCl_4^{2-}$ does not show a band below 40 trcm, although the corresponding band in the experimental absorption spectrum is present and no different in shape and relative intensity to the second peak than for the other $d^8$ complexes. This may be due to a limitation in the experimental recording technique. The PT2//CI (and TD-KST as well) $PdCl_4^{2-}$ absorption spectrum (Figure 2) matches well the experimental spectrum and allows for a similar assignment of the absorption shoulder and corresponding MCD band as for the other $d^8$ complexes.

The intense second $^1E_u$ absorption seen for all $d^8$ complexes goes along with a large positive $\mathcal{A}$-term in the MCD spectrum. The calculations nicely reproduce the negative-positive derivative-peak pattern seen in the experimental MCD spectra above 35 trcm. In the calculations, the positive $\mathcal{A}$ term is accompanied by a negative $\mathcal{B}$ term, such that the intensity of the derivative band shape is reinforced at low energy and weakened at high energy. In the experimental spectra, $PdCl_4^{2-}$ and $AuBr_4^-$ exhibit the clearest evidence of the $\mathcal{A}$-term derivative band shape distortion due to a negative $\mathcal{B}$ term, while $AuCl_4^-$ shows the opposite behavior. It is presently unclear if the vibronic fine structure underlying the MCD bands, or explicit interactions with the solvent, both of which were not explicitly modeled, are responsible for this discrepancy.

Table 1: Calculated vs. experimental absorption energies, oscillator strengths and MCD terms for the various $d^8$ complexes.[a]

| | | PT2//CI | | | | Expt.[70] | | |
|---|---|---|---|---|---|---|---|---|
| | | $\Delta E$ | $f^b$ | $\mathcal{A}$ | $\mathcal{B}$ | | $\Delta E$ | $\mathcal{A}$ |
| $PdCl_4^{2-}$ | $^1E_u$ ($2e_u$) | 34086 | 0.362 | −3.20 | 456.89 | $^1A_{2u}$+$^1E_u$ | 35800 | |
| | $^1A_{2u}$ ($1b_{2u}$) | 34927 | 0.000[c] | 0.00 | 10.78 | | | |
| | $^1E_u$ ($1e_u$) | 44496 | 1.464 | 15.79 | −518.18 | $^1E_u$ | 44900 | 7.27 |
| $PdBr_4^{2-}$ | $^1E_u$ ($2e_u$) | 31035 | 0.383 | −3.37 | 528.99 | $^1A_{2u}$+$^1E_u$ | 30100 | |
| | $^1A_{2u}$ ($1b_{2u}$) | 31971 | 0.000[c] | 0.00 | −12.32 | | | |
| | $^1E_u$ ($1e_u$) | 42423 | 1.377 | 16.01 | −575.95 | $^1E_u$ | 40500 | 5.40 |
| $AuCl_4^-$ | $^1A_{2u}$ ($1b_{2u}$) | 29907 | 0.000[c] | 0.00 | 23.98 | $^1A_{2u}$+$^1E_u$ | 32000 | |
| | $^1E_u$ ($2e_u$) | 30268 | 0.179 | −0.44 | 301.61 | | | |
| | $^1E_u$ ($1e_u$) | 44879 | 1.578 | 9.80 | −319.81 | $^1E_u$ | 44500 | 6.20 |
| $AuBr_4^-$ | $^1E_u$ ($2e_u$) | 26704 | 0.188 | −0.15 | 622.86 | $^1A_{2u}$+$^1E_u$ | 26200 | |
| | $^1A_{2u}$ ($1b_{2u}$) | 26876 | 0.000[c] | 0.00 | −247.17 | | | |
| | $^1E_u$ ($1e_u$) | 41902 | 1.695 | 10.70 | −369.68 | $^1E_u$ | 39500 | 6.10 |

[a] $\Delta E$ in photon wavenumbers ($cm^{-1}$). $\mathcal{A}$ in Debye$^2$. $\mathcal{B}$ in Debye$^2$ per Hartree. The main orbital excitation is noted between parentheses; the acceptor orbital is always $2b_{1g}$. [b]RAS-CI oscillator strengths. [c]The small oscillator strengths were calculated to be: $5.23\cdot10^{-6}$ ($PdCl_4^{2-}$), $6.03\cdot10^{-6}$ ($PdBr_4^{2-}$), $5.35\cdot10^{-6}$ ($AuCl_4^-$), and $1.42\cdot10^{-4}$ ($AuBr_4^-$)

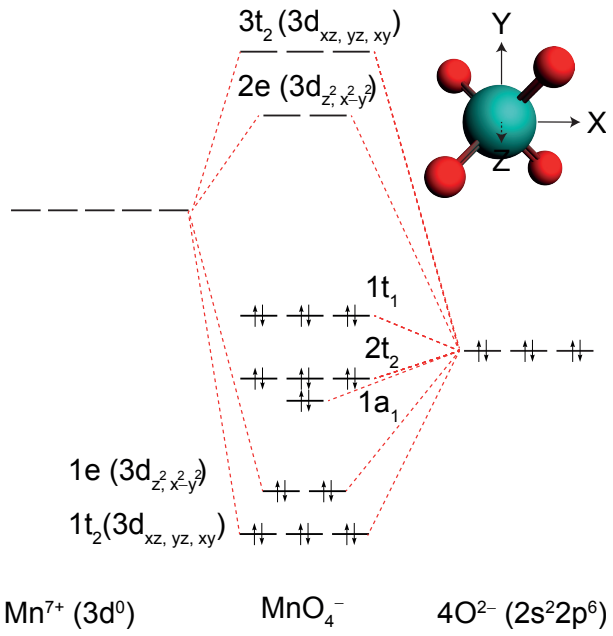


Figure 4: Valence MO diagram for $MnO_4^-$. The MO levels were obtained from KST and are drawn to scale. Symmetry labels according to the $T_d$ point group. Selected metal-ligand bonding and antibonding MOs are labeled according to the contributing metal orbital.

### 3.2 Absorption and MCD spectrum of $MnO_4^-$

A qualitative valence MO diagram for $MnO_4^-$ is shown in Figure 4. Iso-surfaces for the corresponding MOs, converged in RAS, are shown in Figure S3. In the $T_d$ LF, the 3d orbitals of Mn overlap with the O 2p orbitals in irreps e and $t_2$, forming sets of bonding (filled) and antibonding (unoccupied) $1t_2(\sigma)/3t_2(\sigma^*)$ and $1e(\pi)/2e(\pi^*)$ MOs. Energetically in between these MOs, there are ligand-centered MOs ($1a_1$, $2t_2$ and $1t_2$) of mostly O 2p character. The $MnO_4^-$ GS is a closed-shell spin-singlet $^1A_1$.

The low-energy absorption spectrum of $MnO_4^-$ reveals three electronic excitations below 40 trcm.

Table 2: Calculated vs. experimental absorption energies, oscillator strengths and MCD terms for $MnO_4^-$.[a] TD-KST data is placed in Table S4.

| | RAS-SCF | | | | Expt.[75b] | | |
|---|---|---|---|---|---|---|---|
| | ΔE | $f$ | $\mathcal{A}$ | $\mathcal{B}$ | ΔE | $\mathcal{A}$ | $\mathcal{B}$ |
| $1t_1 \rightarrow 2e$ | 21799 | 0.012 | −0.26 | −6.01 | 19050 | −0.55 | −24.55 |
| $1t_1, 2t_2 \rightarrow 2e$ | 31153 | 0.004 | 0.01 | 2.49 | | | |
| $1t_1, 2t_2 \rightarrow 2e, 3t_2$ | 36447 | 0.010 | 0.24 | −12.26 | | 1.00 | −2.18 |

[a] $\Delta E$ in photon wavenumbers ($cm^{-1}$). $\mathcal{A}$ in $D^2$ (D = Debye). $\mathcal{B}$ in $D^2$ per Hartree. [b] The experimentally reported $\mathcal{B}$-term values were converted to au and modern conventions by Seth et al.[37] The listed values are those of Seth et al. after conversion to $D^2$

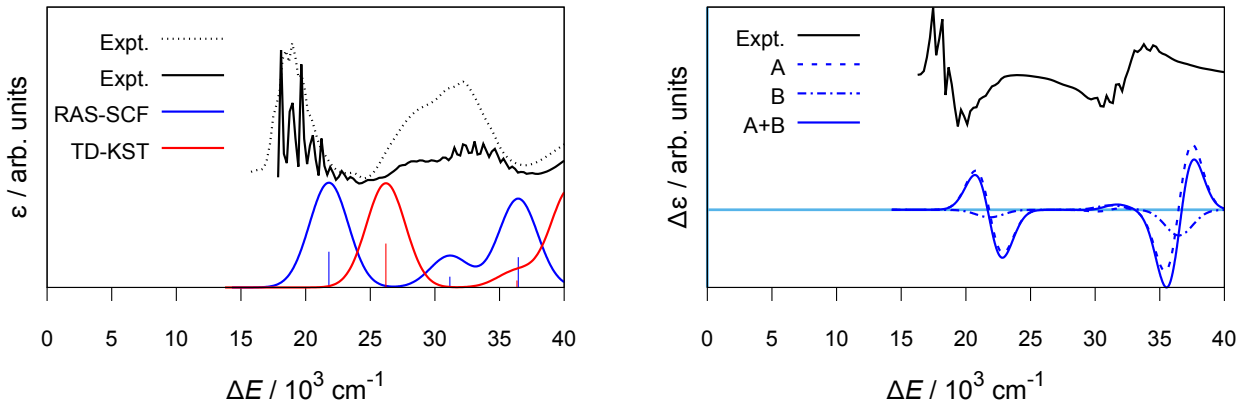


Figure 5: Calculated vs. experimental[75] absorption (left) and MCD (right) spectrum of $MnO_4^-$. The gas-phase absorption spectrum is shown with black dotted line.[75] The spectra were produced with a Gaussian broadening of 1000 $cm^{-1}$ for the individual transitions.

The spectrum has been studied experimentally in gas phase,[76] aqueous solution,[76,77] and in the solid state.[77] The absorption bands are due to dipole-allowed $^1A_1 \rightarrow {}^1T_2$ allowed transitions. The gas phase spectrum displays a rich vibronic fine structure for the lowest and the third transition, and much less so in solution. The vibronic bands have been modeled elsewhere,[78,79] and we focus here on the main electronic features and the MCD. The band positions do not vary strongly between the gas phase, liquid phase, and solid state. The first band is centered around 17.5 trcm in the gas phase spectrum, 18 – 20 trcm in the aqueous phase, and 19.4 trcm in the condensed phase. The second transition appears as a shoulder at 28.6 trcm in gas phase, 28 trcm in the aqueous phase, and 29 trcm in the condensed phase. The third band peaks at 31.8 trcm in gas phase, 32 trcm in the aqueous phase, and 33 trcm in the condensed phase. Several previous computational studies[67,68,76,80] have also shown that the electronic valence excitation energies of $MnO_4^-$ are not very sensitive to the environment of the complex. Our own TD-KST calculations without and with a solvent model for water gave very similar absorption spectra as well (see Figure S6). Therefore, the RAS-level calculations for the absorption and MCD spectrum of $MnO_4^-$ were performed only in gas phase, while comparison will be made with data measured for dissolved $KMnO_4$.

The calculated and experimental $MnO_4^-$ absorption spectra are shown in Figure 5. It is worth noting that both RAS-SCF and TD-KST reproduce the experimental spectrum qualitatively correctly, with RAS-SCF giving better agreement for the band positions. PT2 calculations were not performed. Sharma et al. reported recently that PT2 does not give an improvement for the three transitions of interest.[68] Moreover, several authors have discussed the compositions of the ground and low-lying excited states of $MnO_4^-$ in detail in recent years,[67,68,79] and therefore we provide only a brief commentary. The accepting orbital for the three lowest dipole-allowed transitions is either the 2e LUMO or the $3t_2$ LUMO+1, and the resulting excited states are strongly multicon-

figurational. The first transition is $1t_1 \rightarrow 2e$ in both the RAS-SCF and TD-KST calculations. With TD-KST, the second transition is 70% $2t_2 \rightarrow 2e$ and 25% $1t_1 \rightarrow 3t_2$. Inspection of the RAS-SCF wavefunctions in terms of orbital natural occupations (see Table S3) assigns the second transition mainly as a mixture of $1t_1$, $2t_2 \rightarrow 2e$. The third transition is primarily $1t_1 \rightarrow 3t_2$ with both RAS-SCF (Table S3) and TD-KST (65% $1t_1 \rightarrow 3t_2$ and 23% $2t_2 \rightarrow 2e$).

The calculated RAS-SCF and an experimental MCD spectrum are shown in Figure 5. Numerical data are provided in Table 2. Since $MnO_4^-$ has a closed-shell GS, there are no $\mathcal{C}$-terms. $\mathcal{B}$-terms could be important and therefore a number of additional excited states were accounted for in the RAS-SCF calculations to ensure the $\mathcal{B}$-term SOS convergence. Apart from the missing vibrational fine-structure, can be obtained at the Franck-Condon level,[79] the calculated MCD spectrum is seen to be rather accurate. The RAS+SO MCD spectrum shows two prominent $\mathcal{A}$-terms and two small over-shadowed $\mathcal{B}$-terms associated with the first and third electronic transitions, mainly $1t_1 \rightarrow 2e$. Below the second $\mathcal{A}$-term signal, a weak positive MCD band is associated with the second electronic transition. Its band shape and sign is dominated by a positive $\mathcal{B}$-term. The peak is weakly resolved in the calculated spectrum, while it is effectively absent from the experimental MCD spectrum.

### 3.3 Absorption and MCD spectra of $d^9$ complexes

A valence MO diagram representative of the two studied Cu complexes is shown in Figure 6. Isosurfaces of the relevant MOs, obtained at the RAS-level, are shown in Figure S2. In the non-planar $D_{2d}$ LF, the Cu 3d orbitals are split into $b_1$, $a_1$ and e doubly-occupied species, and an antibonding $3b_2$ orbital which is singly-occupied. Unlike the $3b_2$ orbital and its bonding counterpart $1b_2$, which show strong metal-ligand mixing ($\sigma$ bonding and $\sigma^*$ antibonding), the other Cu 3d orbitals are localized on the metal center, especially in the RAS calculations. Besides the non-planarity of the complexes, the d orbital splitting is quite similar to the more commonly studied $D_{4h}$ $Cu^{2+}$ complexes.[81,82] The electronic GS is a spin-doublet $^2B_2$ and spatially non-degenerate in the absence of SOC. The experimental MCD spectra were recorded at low temperature and assigned to $\mathcal{C}$ terms. As $\mathcal{C}$ terms require the presence of a spatial degeneracy in the GS, all calculations were performed with the inclusion of SOC.

For the $^2B_2$ GS in $D_{2d}$ symmetry, the only dipole-allowed transitions are to $^2E$ and $^2A_1$ states. The singly-occupied $3b_2$ orbital is the acceptor orbital in the low-energy one-electron excitations from the ligand-centered MOs. The measured and calculated absorption spectra are shown in Figure 7. Numerical data with state assignments are collected in Tables S5, S6 and S7. The measured absorption spectra display three main bands, in some cases with structure, stretching from 21 trcm to 42 trcm for $CuCl_4^{2-}$, and from around 19 trcm to 37 trcm for $CuBr_4^{2-}$. Our PT2//CI+SO

and TD-KST+SO calculations both reproduce the energetic positions of the bands, while TD-KST+SO delivers better intensities than PT//CI+SO. The PT2 dynamic correlation effects are critical in delivering physically meaningful band positions. Rivoal et al. discussed the bands at length and correctly assigned the various absorption bands.[83] For both $Cu^{2+}$ complexes, the first two absorption bands involve transitions from the $^2B_2$ GS to $^2E$ states or SO states of $^2E$, $^2B_1$ and $^2B_2$ character. The third absorption band is exclusively assigned as transitions to $^2A_1$ states. Plots of the measured and calculated MCD spectra for the Cu complexes are shown in Figure 7. Numerical data are collected in Table 3. With SOC, the Kramers doublet GS of each Cu complex acquires a degree of spatial degeneracy by mixing with components of spatially degenerate states. This allows for the presence of $\mathcal{C}$ terms that end up dominating the MCD spectra at low temperature. The experimental spectra were recorded at 7.5 and 23 K, respectively. Test calculations delivered $\mathcal{A}$ terms that were orders of magnitude smaller than the $\mathcal{C}$ terms at these temperatures. No further attempt was made to calculate $\mathcal{B}$ terms since they are very likely to be of the same order of magnitude as the $\mathcal{A}$ terms. Consequently, only $\mathcal{C}$ terms were calculated with PT2//CI+SO.

The computed PT2//CI+SO $\mathcal{C}$-term spectra captures the major measured spectral features reasonably well. The experimental spectra for the two complexes are similar in the energy range of the second absorption band, where three $\mathcal{C}$-terms, two negative and one positive, can be distinguished. For $CuCl_4^{2-}$ these three $\mathcal{C}$ terms are generated solely by transitions to $^2E$ states (Table S6).

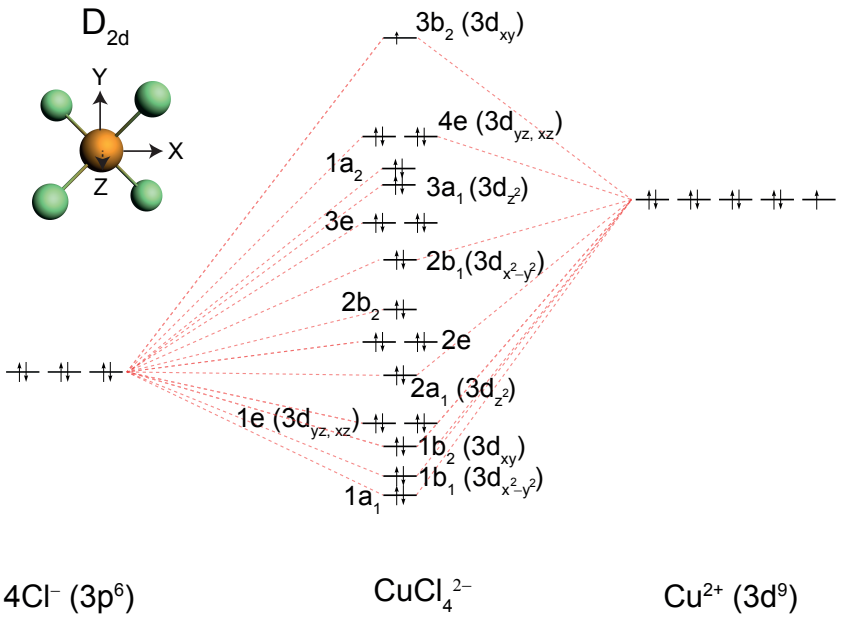


Figure 6: Valence MO diagram for $CuCl_4^{2-}$. The MO levels were obtained from (restricted open-shell) KST and are drawn to scale. Symmetry labels according to the $D_{2d}$ point group. Selected metal-ligand bonding and antibonding MOs are labeled according to the contributing metal orbital.

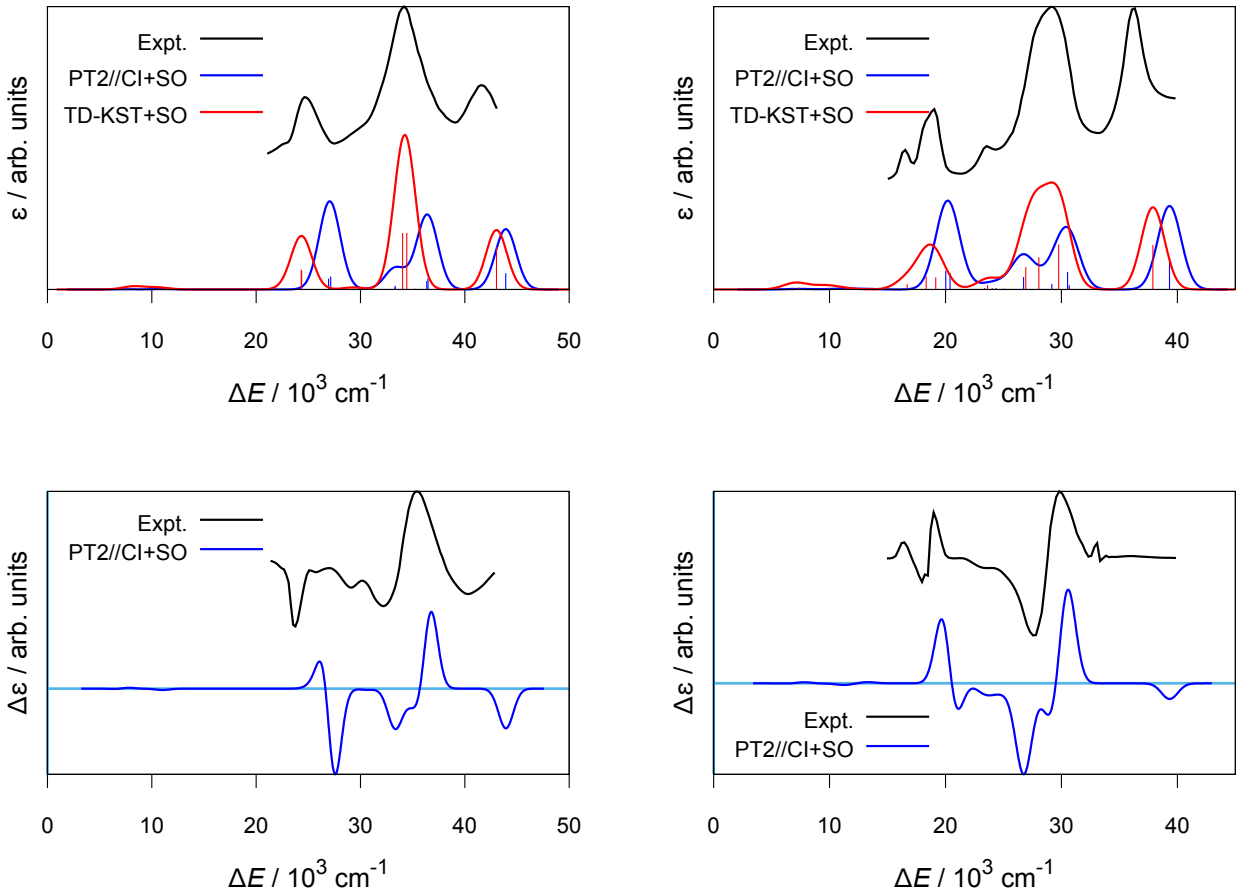


Figure 7: Calculated vs. experimental[83] absorption (top) and MCD (bottom, $\mathcal{C}$-terms only for the calculations) spectra for $CuCl_4^{2-}$ (left) and $CuBr_4^{2-}$ (right). The calculated spectra were produced with a Gaussian broadening of 1000 $cm^{-1}$ for the individual transitions.

Table 3: PT2//CI+SO calculated excitation energies, oscillator strengths and MCD $\mathcal{C}$-terms for various SO states of the $d^9$ complexes.[a]

| $CuCl_4^{2-}$ | | | | $CuBr_4^{2-}$ | | | |
|---|---|---|---|---|---|---|---|
| State | ΔE | $f^b$ | $\mathcal{C}$ | State | ΔE | $f^b$ | $\mathcal{C}$ |
| $1^2E$ | 26942 | 0.045 | 0.83 | $1^2E$ | 20016 | 0.050 | 1.27 |
| $1^2E$ | 27146 | 0.068 | −0.99 | $1^2E+2^2B_2$ | 20394 | 0.063 | −0.98 |
| $2^2E$ | 33321 | 0.009 | −0.23 | $2^2B_2+1^2E$ | 23382 | 0.013 | −0.07 |
| $2^2E$ | 33330 | 0.009 | 0.13 | $2^2E+3^2B_2$ | 26732 | 0.006 | −0.57 |
| $3^2E$ | 36352 | 0.016 | −0.48 | $3^2E+1^2B_1$ | 29171 | 0.012 | −0.24 |
| $3^2E$ | 36470 | 0.035 | 0.65 | $3^2E$ | 30527 | 0.017 | 0.72 |
| $1^2A_1$ | 43925 | 0.050 | −0.08 | $1^2B_1+3^2E$ | 30674 | 0.051 | −0.17 |
| | | | | $1^2A_1$ | 39321 | 0.007 | −0.08 |

[a] $\Delta E$ in photon wavenumbers ($cm^{-1}$). $\mathcal{C}$ in $Debye^2$. Detailed state assignments are provided in Tables S5 and S6. TD-KST+SO data is shown in Table S7. [b]RAS-CI+SO oscillator strengths.

The same $^2$E states are also responsible for the three $\mathcal{C}$ terms in the $CuBr_4^{2-}$ case, although there are some minor contributions from $^2B_1$ and $^2B_2$ states in the calculation. In the energy region of the first absorption band, there are also three $\mathcal{C}$-terms, two positive and one negative. The experimental $CuCl_4^{2-}$ spectrum shows only the negative $\mathcal{C}$-term, but further analysis by Rivoal et al.[83] (gaussian analysis of room vs. low-temperature absorption and MCD spectra) suggested that the two positive $\mathcal{C}$ terms should be present as well at 22.8 and 25 trcm. The computed PT2//CI+SO spectra capture well only the first positive $\mathcal{C}$-term (caused by transitions to $^2$E states, Table 3 and S6) and the negative $\mathcal{C}$-term (caused by transitions to $^2$E states for $CuCl_4^{2-}$ and transitions to $^2$E and $^2B_2$ for $CuBr_4^{2-}$) for both complexes. The second positive $\mathcal{C}$-term does not create a resolved band in the broadened PT2//CI+SO spectrum due to low intensity. Finally, in the energetic region of the third absorption band, negative $\mathcal{C}$-terms due to transitions to $^2A_1$ states are obtained with PT2//CI+SO. This is in agreement with the measured spectrum for the $CuCl_4^{2-}$ complex, which exhibits negative MCD at 40 trcm. The calculation for $CuBr_4^{2-}$ gives a corresponding minor negative peak at the energy range of the third absorption band. The experimental MCD spectrum is nearly featureless at the energies where the third absorption peak occurs, with a very weak +/- sign pattern toward the high-energy cut-off of the spectrum.

### 3.4 Absorption and MCD spectrum of $Fe(CN)_6^{3-}$

The octahedral $d^5$ complex $Fe(CN)_6^{3-}$ is a textbook example for MCD[1] – but complicated – and challenging for calculations. Due to the large effects of the dynamic correlation on the LMCT state energies, red shifting them by several electron volts, Ganyushin and Neese (GN) used a sophisticated approach combining spin-free difference-dedicated CI (DDCI) and a finite-field (FF) difference spin-orbit multi-reference CI to calculate the MCD spectrum.[46] The FF approach for the magnetic field does not straightforwardly give $\mathcal{A}$, $\mathcal{B}$, and $\mathcal{C}$ individually and requires an isotropic averaging via a numerical grid. But it can be used for simulations beyond the linear perturbation regime for the magnetic field, for example to simulate variable temperature & field data at fixed incident wavelengths (VTVH MCD).[2,3] Therefore, the approaches by GN and us are in a sense complementary.

Unlike $CuCl_4^{2-}$ and $CuBr_4^{2-}$, the $O_h$ ground state of $Fe(CN)_6^{3-}$ is orbitally degenerate and therefore gives rise to a $\mathcal{C}$-term spectrum already in the absence of SOC. But the assignment of the MCD spectrum of this complex has met with some controversy. The entire spectrum was initially thought to be caused by $\mathcal{C}$ terms.[75] Kobayashi et al. observed weak temperature-dependency of the intensities, however, and concluded that the MCD spectrum was predominantly caused by $\mathcal{B}$-terms.[84] In contrast, Gale and McCaffery observed strong correlation between temperature and MCD intensity and concluded, based on supporting theoretical estimates, that the initial assign-

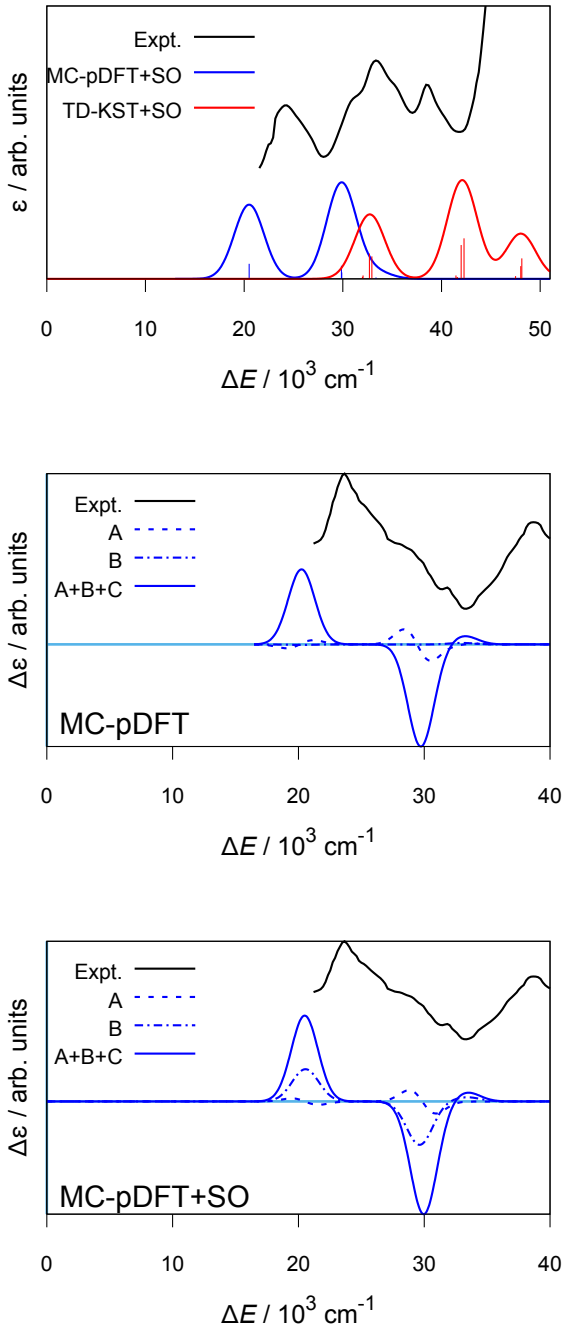


Figure 8: Calculated vs. experimental[75] absorption (top) and MCD (middle and bottom, 300 K) spectrum for $Fe(CN)_6^{3-}$. The spectra were produced with a Gaussian broadening of 1000 $cm^{-1}$ for the individual transitions.

ment was correct.[85,86] Upton and Williamson[87] pointed out that the Kobayashi results may have been due to a poor thermal conductivity of their film sample, while Gale and McCaffery did not consider SO coupling. With SO coupling, Upton and Williamson argued, at 300 K a $\mathcal{B}$-term should cause about half of the MCD intensity of the first band.

The absorption and MCD (300 K) spectra (generated with and without SOC) of $Fe(CN)_6^{3-}$ are shown in Figure 8. The absorption spectrum exhibits three main peaks up to about 40 trcm that are assigned to LMCT transitions $T_{2g} \rightarrow T_{1u}$ and $T_{2u}$. SOC is important for this system but does not influence the absorption spectrum significantly (See Table 4). The calculated GS zero-field splitting is ~680 $cm^{-1}$ with a SO coupling constant of 227 $cm^{-1}$, in reasonable agreement with the values (483 $cm^{-1}$ and 322 $cm^{-1}$, respectively) calculated by GN based on DDCI spin states and KST orbitals.[46] Bleaney et al. estimated a SO coupling constant of 280 $cm^{-1}$ for this system from magnetic susceptibility measurements.[88] The LMCT transitions predicted by MC-pDFT at 20.5, 29.5, and 32.9 trcm somewhat underestimate the energies determined experimentally by Schatz et al.,[75] (24, 33, and 38.5 trcm). Our PT2 calculations (not shown) produced a similar energy for the first band, but a too large splitting between this and the other bands. The energies obtained via DDCI calculations by GN (27.8, 34.1 and 44.2 trcm) overestimate two of the band energies by a similar amount as MC-pDFT underestimates them. The intensity of the third absorption peak in the MC-pDFT calculation is underestimated, which translates into a too weak MCD intensity for this transition as well (vide infra). A TD-KST calculation with SOC does better in comparison but yields an overall too blue shifted spectrum. Keeping in line with the MCD calculations of GN, solvent effects were introduced only at the structure optimization step.

Without SOC, the calculated MCD spectrum features predominantly $\mathcal{C}$-terms, along with a minor $\mathcal{A}$-term contribution to the second band. The introduction SO coupling creates prominent contributions to both bands from $\mathcal{B}$-terms, enhancing the MCD intensity of each band. The $\mathcal{B}$-term contribution to the first band is not quite as large as the model prediction by Upton and Williamson, but the $\mathcal{B}$ and $\mathcal{C}$ term are indeed of roughly the same magnitude.

Table 4: MC-pDFT+SO calculated excitation energies ($cm^{-1}$) and oscillator strengths, and MCD terms for various LMCT states of $Fe(CN)_6^{3-}$.[a]

| | | ΔE | $f$ | $\mathcal{A}$ | $\mathcal{B}$ | $\mathcal{C}$ |
|---|---|---|---|---|---|---|
| $T_{2g}$ | $E''_g$ | 0 | 0 | | | |
| $T_{1u}$ | $U'_u$ | 20505 | 0.021 | −0.40 | 502.30 | 0.80 |
| $T_{2u}$ | $E'_u$ | 29862 | 0.018 | −1.46 | −4287.08 | −0.94 |
| | $U'_u$ | 29895 | 0.009 | 0.46 | 3835.00 | 0.23 |
| $T_{1u}$ | $U'_u$ | 33358 | 0.002 | −0.01 | 40.02 | 0.05 |

[a] $\Delta E$ in photon wavenumbers ($cm^{-1}$). $\mathcal{A}$, $\mathcal{C}$ in $Debye^2$. $\mathcal{B}$ in $Debye^2$ per Hartree. The $E''_g$, $E'_u$, and $U'_u$ are labellings are from the $O_h$ double group. MC-pDFT-SR and TD-KST+SO data is gathered in Tables S8 and S9.

### 3.5 Conclusions

This work demonstrates the feasibility of multiconfiguational restricted active space (RAS) approaches for the calculation of MCD spectra for transition metal complexes. Experimental $\mathcal{A}$- and $\mathcal{B}$-term spectra for the closed shell complexes $PdCl_4^{2-}$, $PdBr_4^{2-}$, $AuCl_4^-$, $AuBr_4^-$, and $MnO_4^-$ were reproduced reasonably well by these calculations. The MCD calculations for these single-reference systems perform as well or better than (quadratic-response) TD-KST. The $\mathcal{C}$-term spectra for the open-shell complexes $CuCl_4^{2-}$ and $CuBr_4^{2-}$, which require the inclusion of SOC in the calculations, are of comparable quality. The RAS approach has the advantage that complicated multi-reference systems can be treated on an equal footing with single-reference systems, and excited state wavefunctions are explicitly available. The RAS-level MCD spectrum for the multi-reference system $Fe(CN)_6^{3-}$ showed that, due to the importance of spin-orbit coupling, the room temperature MCD spectrum is generated both by $\mathcal{B}$- and $\mathcal{C}$-terms, in agreement with model predictions for this system.

In the present approach, the $\mathcal{B}$ terms are obtained via a SOS expansion. We found that for our test systems the expansion converges reasonably quickly, and the quality of the description of states beyond those contributing to the UV-Vis spectral range does not appear to be overly critical. Therefore a RAS-SCF calculation employing a computationally affordable active space may be initially performed to obtain an accurate description of the transitions of interest. The converged wavefunction may subsequently be used as a reference in RAS-CI calculations with larger active spaces, in order to generate additional states used to describe the $\mathcal{B}$-terms without deteriorating the description of the valence states of interest. MC-pDFT calculations appear to be suitable to account for the effects of the dynamic correlation on the state energies in an efficient manner.

## Author information

[†]Y.H. and D.-C.S. contributed equally to this work.

## Conflicts of interest

There are no conflicts to declare.

## Acknowledgments

This work has been supported by grant CHE-1560881 from the National Science Foundation. We thank the Center for Computational Research (CCR) in Buffalo for providing computational

resources, in particular those made available via grant MRI-1724891 from the National Science Foundation.

## Electronic Supplementary Information

The supporting information file contains additional information on optimized structures, RAS-level converged natural orbitals, calculated absorption energies with TD-KST, PT2//SCF and/or RAS-(CI)SCF, and additional MCD spectra plots.

## References

[1] S. B. Piepho and P. N. Schatz, *Group theory in spectroscopy. With applications to magnetic circular dichroism.*, John Wiley & Sons, New York, 1983.

[2] F. Neese and E. I. Solomon, *Inorg. Chem.*, 1999, **38**, 1847–1865.

[3] F. Neese and E. I. Solomon, *J. Am. Chem. Soc.*, 1998, **120**, 12829–12848.

[4] M. Sundararajan, D. Ganyushin, S. Ye and F. Neese, *Dalton Trans.*, 2009, 6021–6036.

[5] F. Paulat and N. Lehnert, *Inorg. Chem.*, 2008, **47**, 4963–4976.

[6] S. Ye, C. Kupper, S. Meyer, E. Andris, R. Navrátil, O. Krahe, B. Mondal, M. Atanasov, E. Bill, F. Roithová, J.and Meyer and F. Neese, *J. Am. Chem. Soc.*, 2016, **138**, 14312–14325.

[7] J. L. Kneebone, V. E. Fleischauer, S. L. Daifuku, A. A. Shaps, J. M. Bailey, T. E. Iannuzzi and M. L. Neidig, *Inorg. Chem.*, 2016, **55**, 272–282.

[8] K. L. Fillman, J. A. Przyojski, M. H. Al-Afyouni, Z. Tonzetich and M. L. Neidig, *Chem. Sci.*, 2015, **6**, 1178–1188.

[9] S. L. Daifuku, M. H. Al-Afyouni, B. E. R. Snyder, J. L. Kneebone and M. L. Neidig, *J. Am. Chem. Soc.*, 2014, **136**, 9132–9143.

[10] S. L. Daifuku, J. L. Kneebone, B. E. R. Snyder and M. L. Neidig, *J. Am. Chem. Soc.*, 2015, **137**, 11432–11444.

[11] N. V. Karimova and C. M. Aikens, *J. Phys. Chem. A*, 2016, **120**, 9625–9635.

[12] N. V. Karimova and C. M. Aikens, *J. Phys. Chem. C*, 2017, **121**, 19478–19489.

[13] S. Vandendriessche, S. Van Cleuvenbergen, P. Willot, G. Hennrich, M. Srebro, V. Valev, G. Koeckelberghs, K. Clays, J. Autschbach and T. Verbiest, *Chem. Mater.*, 2013, **25**, 1139–1143.

[14] J. Mack, Y. Morita, S. Higashibayashi, H. Sakurai and N. Kobayashi, *Chem. Phys. Lett.*, 2013, **556**, 188–194.

[15] T. M. Baker, T. G. Nakashige, E. M. Nolan and M. L. Neidig, *Chem. Sci.*, 2017, **8**, 1369–1377.

[16] P.-P. Wei, A. J. Skulan, N. Mitic, Y.-S. Yang, L. Saleh, J. M. Bollinger Jr. and E. I. Solomon, *J. Am. Chem. Soc.*, 2004, **126**, 3777–3788.

[17] M. L. Neidig and E. I. Solomon, *Chem. Commun.*, 2005, 5843–5863.

[18] M. D. Liptak and T. C. Brunold, *J. Am. Chem. Soc.*, 2006, **128**, 9144–9156.

[19] R. P. Mtei, G. Lyashenko, B. Stein, N. Rubie, R. Hille and M. L. Kirk, *J. Am. Chem. Soc.*, 2011, **133**, 9762–9774.

[20] K. M. Lancaster, M.-E. Zaballa, S. Sproules, M. Sundararajan, S. DeBeer, J. H. Richards, A. J. Villa, F. Neese and H. B. Gray, *J. Am. Chem. Soc.*, 2012, **134**, 8241–8253.

[21] R. E. Linder, E. Bunnenberg, L. Seamans and A. Moscowitz, *J. Chem. Phys.*, 1974, **60**, 1943–1951.

[22] N. Lin, H. Solheim, X. Zhao, F. Santoro and K. Ruud, *J. Chem. Theory Comput.*, 2013, **9**, 1557–1567.

[23] V. Andrushchenko, D. Padula, E. Zhivotova, S. Yamamoto and P. Bour, *Chirality*, 2014, **26**, 655–662.

[24] Y. Kitagawa, S. Wada, K. Yanagisawa, T. Nakanishi, K. Fushimi and Y. Hasegawa, *Chem. Phys. Chem.*, 2016, **17**, 845–849.

[25] R. G. Denning, T. R. Snellgrove and D. R. Woodwark, *Mol. Phys.*, 1976, **32**, 419–442.

[26] R. G. Denning, D. N. P. Foster, T. R. Snellgrove and D. R. Woodwark, *Mol. Phys.*, 1979, **37**, 1089–1107.

[27] C. Görller-Walrand, S. De Houwer, L. Fluyt and K. Binnemans, *Phys. Chem. Chem. Phys.*, 2004, **6**, 3292–3298.

[28] R. G. Denning, J. O. W. Norris and D. Brown, *Mol. Phys.*, 1982, **46**, 287.

[29] R. G. Denning, J. O. W. Norris and D. Brown, *Mol. Phys.*, 1982, **46**, 325.

[30] F. Gendron, V. E. Fleischauer, T. J. Duignan, B. L. Scott, M. W. Löble, S. K. Cary, S. Kozimor, H. Bolvin, M. L. Neidig and J. Autschbach, *Phys. Chem. Chem. Phys.*, 2017, **19**, 17300–17313.

[31] A. D. Buckingham and P. J. Stephens, *Annu. Rev. Phys. Chem.*, 1966, **17**, 399–432.

[32] P. J. Stephens, *J. Chem. Phys.*, 1970, **52**, 3489–3516.

[33] K.-M. Lee, K. Yabana and G. F. Bertsch, *J. Chem. Phys.*, 2011, **134**, 144106.

[34] M. Seth, T. Ziegler, A. Banerjee, J. Autschbach, S. J. A. van Gisbergen and E. J. Baerends, *J. Chem. Phys.*, 2004, **120**, 10942–10954.

[35] M. Seth, M. Krykunov, T. Ziegler, J. Autschbach and A. Banerjee, *J. Chem. Phys.*, 2008, **128**, 144105.

[36] M. Krykunov, M. Seth, T. Ziegler and J. Autschbach, *J. Chem. Phys.*, 2007, **127**, 244102.

[37] M. Seth, M. Krykunov, T. Ziegler and J. Autschbach, *J. Chem. Phys.*, 2008, **128**, 234102.

[38] H. Solheim, K. Ruud, S. Coriani and P. Norman, *J. Phys. Chem. A*, 2008, **112**, 9615–9618.

[39] M. Seth and T. Ziegler, *Chem. Phys.*, 2012, **395**, 63–74.

[40] M. Seth and T. Ziegler, *Adv. Inorg. Chem.*, 2010, **62**, 41–109.

[41] M. S. Nørby, S. Coriani and J. Kongsted, *Theor. Chem. Acc.*, 2018, **137**, 49.

[42] S. Coriani, P. Jørgensen, A. Rizzo, K. Ruud and J. Olsen, *Chem. Phys. Lett.*, 1999, **300**, 61–68.

[43] M. Seth, T. Ziegler and J. Autschbach, *J. Chem. Phys.*, 2005, **122**, 094112.

[44] M. Seth, T. Ziegler and J. Autschbach, *J. Chem. Phys.*, 2008, **129**, 104105.

[45] H. Bolvin, *Inorg. Chem.*, 2007, **46**, 417–427.

[46] D. Ganyushin and F. Neese, *J. Chem. Phys.*, 2008, **128**, 114117.

[47] S. Ye, G. Xue, I. Krivokapic, T. Petrenko, E. Bill, L. Que Jr and F. Neese, *Chem. Sci.*, 2015, **6**, 2909–2921.

[48] E. van Lenthe and E. J. Baerends, *J. Comput. Chem.*, 2003, **24**, 1142–1156.

[49] E. van Lenthe, E. J. Baerends and J. G. Snijders, *J. Chem. Phys.*, 1993, **99**, 4597–4610.

[50] E. J. Baerends, T. Ziegler, A. J. Atkins, J. Autschbach, D. Bashford, O. Baseggio, A. Bérces, F. M. Bickelhaupt, C. Bo, P. M. Boerritger, L. Cavallo, C. Daul, D. P. Chong, D. V. Chulhai, L. Deng, R. M. Dickson, J. M. Dieterich, D. E. Ellis, M. van Faassen, A. Ghysels, A. Giammona, S. J. A. van Gisbergen, A. Goez, A. W. Götz, S. Gusarov, F. E. Harris, P. van den Hoek, Z. Hu, C. R. Jacob, H. Jacobsen, L. Jensen, L. Joubert, J. W. Kaminski, G. van Kessel, C. König, F. Kootstra, A. Kovalenko, M. Krykunov, E. van Lenthe, D. A. McCormack, A. Michalak, M. Mitoraj, S. M. Morton, J. Neugebauer, V. P. Nicu, L. Noodleman, V. P. Osinga, S. Patchkovskii, M. Pavanello, C. A. Peeples, P. H. T. Philipsen, D. Post, C. C. Pye, H. Ramanantoanina, P. Ramos, W. Ravenek, J. I. Rodríguez, P. Ros, R. Rüger, P. R. T. Schipper, D. Schlüns, H. van Schoot, G. Schreckenbach, J. S. Seldenthuis, M. Seth, J. G. Snijders, M. Solà, S. M., M. Swart, D. Swerhone, G. te Velde, V. Tognetti, P. Vernooijs, L. Versluis, L. Visscher, O. Visser, F. Wang, T. A. Wesolowski, E. M. van Wezenbeek, G. Wiesenekker, S. K. Wolff, T. K. Woo and A. L. Yakovlev, *ADF2017, SCM, Theoretical Chemistry, Vrije Universiteit, Amsterdam, The Netherlands, https://www.scm.com*.

[51] T. Yanai, D. P. Tew and N. C. Handy, *Chem. Phys. Lett.*, 2004, **393**, 51–57.

[52] M. Douglas and N. M. Kroll, *Ann. Phys.*, 1974, **82**, 89–155.

[53] B. A. Hess, *Phys. Rev. A*, 1985, **32**, 756–763.

[54] B. A. Hess, *Phys. Rev. A*, 1986, **33**, 3742–3748.

[55] A. Wolf, M. Reiher and B. A. Hess, *J. Chem. Phys.*, 2002, **117**, 9215–9226.

[56] B. O. Roos, R. Lindh, P.-Å. Malmqvist, V. Veryazov and P.-O. Widmark, *Chem. Phys. Lett.*, 2005, **409**, 295–299.

[57] B. O. Roos, R. Lindh, P.-Å. Malmqvist, V. Veryazov and P.-O. Widmark, *J. Phys. Chem. A*, 2004, **108**, 2851–2858.

[58] F. Aquilante, J. Autschbach, R. K. Carlson, L. F. Chibotaru, M. G. Delcey, L. D. Vico, I. Fdez. Galván, N. Ferré, L. M. Frutos, L. Gagliardi, M. Garavelli, A. Giussani, C. E. Hoyer, G. L. Manni, H. Lischka, D. Ma, P.-Å. Malmqvist, T. Müller, A. Nenov, M. Olivucci, T. B. Pedersen, D. Peng, F. Plasser, B. Pritchard, M. Reiher, I. Rivalta, I. Schapiro, J. Segarra-Martí, M. Stenrup, D. G. Truhlar, L. Ungur, A. Valentini, S. Vancoillie, V. Veryazov, V. P. Vysotskiy, O. Weingart, F. Zapata and R. Lindh, *J. Comput. Chem.*, 2016, **37**, 506–541.

[59] M. Cossi, N. Rega, G. Scalmani and V. Barone, *J. Chem. Phys.*, 2001, **114**, 5691–5701.

[60] V. Barone and M. Cossi, *J. Phys. Chem. A*, 1998, **102**, 1995–2001.

[61] K. Andersson, P.-Å. Malmqvist, B. O. Roos, A. J. Sadlev and K. Wolinski, *J. Phys. Chem.*, 1990, **94**, 5483–5488.

[62] L. Gagliardi, D. G. Truhlar, G. Li Manni, R. K. Carlson, C. E. Hoyer and J. L. Bao, *Acc. Chem. Res.*, 2017, **50**, 66–73.

[63] C. van Wüllen and W. Kutzelnigg, *Chem. Phys. Lett.*, 1993, **205**, 563–571.

[64] S. M. Cybulski and D. M. Bishop, *J. Chem. Phys.*, 1994, **100**, 2019–2026.

[65] F. Gendron, B. Le Guennic and J. Autschbach, *Inorg. Chem.*, 2014, **53**, 13174–13187.

[66] S. Vancoillie and K. Pierloot, *J. Phys. Chem. A*, 2008, **112**, 4011–4019.

[67] J. Su, W.-H. Xu, C.-F. Xu, W. Schwarz and J. Li, *Inorg. Chem.*, 2013, **52**, 9867–9874.

[68] P. Sharma, D. G. Truhlar and L. Gagliardi, *J. Chem. Phys.*, 2018, **148**, 124305.

[69] URL `https://github.com/jautschbach/mcd-molcas.git` (accessed 12/18).

[70] A. McCaffery, P. N. Schatz and P. J. Stephens, *J. Am. Chem. Soc.*, 1968, **90**, 5730–5735.

[71] K. Jørgensen, C, *Adv. Chem. Phys.*, 1963, **5**, 33–146.

[72] H. Basch and H. B. Gray, *Inorg. Chem.*, 1967, **6**, 365–369.

[73] H. B. Gray, Proceedings of the 8th International Conference on Coordination Chemistry, Vienna, 1964, pp. 133–135.

[74] B. G. Anex and N. Takeuchi, *J. Am. Chem. Soc.*, 1974, **96**, 4411–4416.

[75] P. N. Schatz, A. J. McCaffery, W. Suëtaka, G. N. Henning, A. B. Ritchie and P. J. Stephens, *J. Chem. Phys.*, 1966, **45**, 722–734.

[76] J. Houmøller, S. H. Kaufman, K. Støchkel, S. B. Tribedi, L.C. Nielsen and J. M. Weber, *ChemPhysChem*, 2013, **14**, 1133–1137.

[77] S. L. Holt and C. J. Ballhausen, *Theor. Chem. Acc.*, 1967, **7**, 313–320.

[78] J. Neugebauer, E. Jan Baerends, M. Nooijen and J. Autschbach, *J Chem Phys*, 2005, **122**, 234305.

[79] L. Jose, M. Seth and T. Ziegler, *J. Phys. Chem. A*, 2012, **116**, 1864–1876.

[80] J. M. H. Olsen and Hedegád, *Phys. Chem. Chem. Phys.*, 2017, **19**, 15870–15875.

[81] V. Sauri, L. Serrano-Andrés, A. R. M. Shahi, L. Gagliardi, S. Vancoillie and K. Pierloot, *J. Chem. Theory Comput.*, 2011, **7**, 153–168.

[82] K. D. Vogiatzis, G. L. Manni, S. J. Stoneburner, D. Ma and L. Gagliardi, *J. Chem. Theory Comput.*, 2015, **11**, 3010–3021.

[83] J. C. Rivoal and B. Briat, *Mol. Phys.*, 1974, **27**, 1081–1108.

[84] H. Kobayashi, M. Shimizu and Y. Kaizu, *Bull. Chem. Soc. Jpn.*, 1970, **43**, 2321–2325.

[85] R. Gale and M. A. J., *J. C. S. Chem. Comm.*, 1972, 832–833.

[86] R. Gale and A. J. McCaffery, *J. C. S. Dalton*, 1972, 1344–1351.

[87] A. H. P. Upton and B. E. Williamson, *J. Phys. Chem.*, 1994, **98**, 71–76.

[88] B. Bleaney and M. C. M. O'Brien, *Proc. Phys. Soc. London Sect. B*, 1956, **69**, 1216–1230.

## Table of Contents Graphics